Available online at www.sciencedirect.com

ScienceDirect

Defence Technology 12 (2016) 305–315

www.elsevier.com/locate/dt

Numerical simulation and experimental validation of arc welding of DMR-249A steel

Rishi PAMNANI [a,*], M. VASUDEVAN [b], T. JAYAKUMAR [c], P. VASANTHARAJA [b], K.C. GANESH [d]

[a] *Prototype Training Centre, Kalpakkam, Tamil Nadu 603 127, India*
[b] *IGCAR, Tamil Nadu 603 102, India*
[c] *Metallurgical and Materials Engg Dept, NIT, Warangal 506 004, India*
[d] *Dept of Mech Engg, NITT, Tiruchirappalli 620 015, India*

Received 24 October 2015; revised 11 December 2015; accepted 12 January 2016

Available online 2 March 2016

Abstract

The thermo-mechanical attributes of DMR-249A steel weld joints manufactured by shielded metal arc welding (SMAW) and activated gas tungsten arc welding (A-GTAW) processes were studied using Finite Element Model (FEM) simulation. The thermal gradients and residual stresses were analyzed with SYSWELD software using double ellipsoidal heat source distribution model. The numerically estimated temperature distribution was validated with online temperature measurements using thermocouples. The predicted residual stresses profile across the weld joints was compared with the values experimentally measured using non-destructive techniques. The measured and predicted thermal cycles and residual stress profile was observed to be comparable. The residual stress developed in double sided A-GTAW joint were marginally higher in comparison to five pass SMAW joint due to phase transformation associated with high heat input per weld pass for A-GTAW process. The present investigations suggest the applicability of numerical modeling as an effective approach for predicting the thermo-mechanical properties influenced by welding techniques for DMR-249A steel weld joints. The tensile, impact and micro-hardness tests were carried to compare the welds. Considering benefits of high productivity and savings of labor and cost associated with A-GTAW compared to SMAW process, the minor variation in residual stress build up of A-GTAW joint can be neglected to develop A-GTAW as qualified alternative welding technique for DMR-249A steel.

Keywords: DMR-249A; A-GTAW; SMAW; FEM; SYSWELD; Thermo-mechanical Simulation

1. Introduction

DMR-249A is a low carbon HSLA steel. The steel has micro-alloying additions of V, Nb and Ti for grain refinement resulting in increased strength and good impact toughness at sub-zero temperatures. The steel has microstructure of fine equiaxed ferrite with pearlite content of less than 10% by volume [1,2]. The steel is being used in the construction of the hull of various vessels and ships. The conventional arc welding is extensively used during construction and fabrication of ships. The shielded metal arc welding (SMAW) is the most common process used while other arc welding processes also find applications. Though gas tungsten arc welding (GTAW) process produces high quality weld deposits, the limitations of shallow penetration and low productivity are associated with the process. A variant of GTAW process called activated flux gas tungsten arc welding (A-GTAW) has been reported to overcome the limitations of GTAW process. A significant increase in penetration of up to 300% has been reported in with the use of activated flux in GTAW welding [3–5].

The residual stresses (RS) in a component or structure are stresses caused by incompatible internal permanent strains. Welding is one of the significant causes of RS. The measurement of residual stresses developed during welding of a ship's hull helps in lowering risk to failure by predicting the influence of residual stresses on fatigue, corrosion and other detrimental surface phenomena. Tensile residual stresses are harmful as they assist crack propagation and also contribute to fatigue failure and stress corrosion cracking [6,7]. Compressive residual stresses increase wear and corrosion resistance and are beneficial in preventing origination and propagation of fatigue cracks

Peer review under responsibility of China Ordnance Society.
* Corresponding author. Tel.: +91 9445823932.
E-mail address: rishi.rashmi.p@gmail.com (R. PAMNANI).

http://dx.doi.org/10.1016/j.dt.2016.01.012

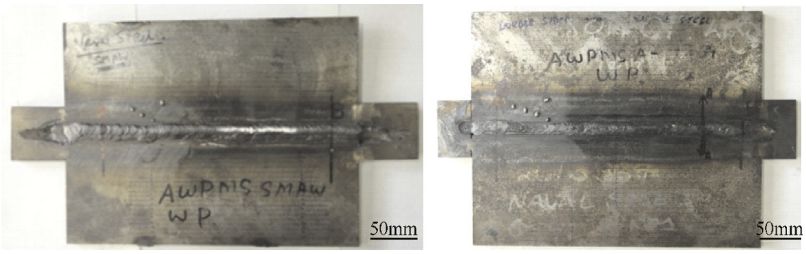

(a) (b)

Fig. 1. Photos of weld joints (a) SMAW (b) A-GTAW.

[8,9]. The prediction of residual stress is important to optimize the welding process for reducing their detrimental effects. The estimation of RS profile across weld joints has been carried out using X-ray diffraction and ultrasonic techniques [10,11].

A lot of research has been undertaken to develop numerical models to understand the effect of heat input and welding process on the weld attributes [12–15]. P. Duranton et al. [16] explained the simulation methodology for thermo-mechanical analysis of multi pass welding. P. Mollicone et al. [17] explained thermo-elasto-plastic stages of the welding process with finite-element (FE) modeling strategies. Srikas et al. [18] carried out research on thermo mechanical simulation of naval structure materials during arc welding. The SYSWELD software has been used to establish FEM analysis as a useful tool in thermo mechanical characterization of welding processes [5,12–18].

The present work involves the finite element modeling of SMAW and A-GTAW processes for DMR-249A steel to predict thermal cycles and residual stresses on 10 mm thick plates and validation by experimental tools. The simulated thermal cycles were validated by thermocouple measurements at specified locations during SMAW multipass welding and autogenous double-sided welding using A-GTAW process. The simulated residual stress profiles were validated by non-destructive testing techniques. The objective of the research study was to establish the applicability of numerical simulation for residual stresses measurements of DMR-249A steel joints and ascertain the variation in residual stresses profile for conventional low heat input SMAW and high productivity A-GTAW technique.

2. Materials and methods

The material composition of the plates used in this study is given below in Table 1 and the welding parameters for weld joints are given in Table 2.

For each weld joint, two plates of dimension $300 \times 120 \times 10$ mm were used and welded to make a weld specimen plate of $300 \times 240 \times 10$ mm with 300 mm weld length. The square butt joint was used for A-GTAW and 70° V-grove butt joint for SMAW (Fig. 1).

The GTAW using activated flux was carried out by using automatic welding machine (Fig. 2). A DCEN power sourced tungsten electrode (2% thoriated) of 3.2 mm diameter with 60° tip angle and shielding gas (Argon) flow rate of 10 l/min was used. The mixture of SiO_2, TiO_2, NiO, CuO_2 and combinations of oxide powders specially developed for DMR-249A steel was used as activated flux [4].

The metallographic samples of size $20 \times 10 \times 10$ mm were cut to carry out microscopic studies of the weld joint. Samples were polished from 80 to 2400 grit SiC paper followed by alumina (sizes 5 μm and 1 μm) suspension to obtain mirror finish. The specimens were etched using 2% Nital solution, and optical microscopy was carried out to ascertain weld bead profile and changes in microstructure of base and weld metal. The microhardness, impact ($55 \times 10 \times 10$ mm^3) and tensile (gauge length 260 mm, gauge diameter 4 mm) tests of the welded joint were conducted as per ASTM Standards E384, E23 and E8 respectively.

Temperature measurements during the welding of butt joints were done with help of K-type thermocouples. The K-type thermocouples were spot welded on the plate before welding at a distance of 10 to 20 mm from the center line (Fig. 2). For double sided A-GTAW, both passes being symmetrical, thermocouples were used to measure temperature profiles for second pass only. For multi pass SMAW, with limited storage capacity for thermocouple data, the time duration between changing of electrodes and removal of slag was not logged. The thermocouple values were used for the validation of thermal cycles obtained from welding model.

Table 1
Chemical composition (wt%) DMR-249A.

C	S	P	Mn	Si	Al	Ni	Nb	V	Ti	B/Cu/Cr	N_2/ppm	Fe
0.09	0.006	0.14	1.55	0.24	0.026	0.72	0.039	0.02	0.019	<0.020	56	Bal.

Table 2
Welding parameters for weld joints.

Welding process	Current/A	Voltage/V	Speed/(mm·s^{-1})	No. of passes	Heat input for weld length/(kJ·mm^{-1})	Heat input for final pass/(kJ·mm^{-1})
A-GTAW	270	20	1	2	10.8	5.4
SMAW	120	25	1.5	5	10	2

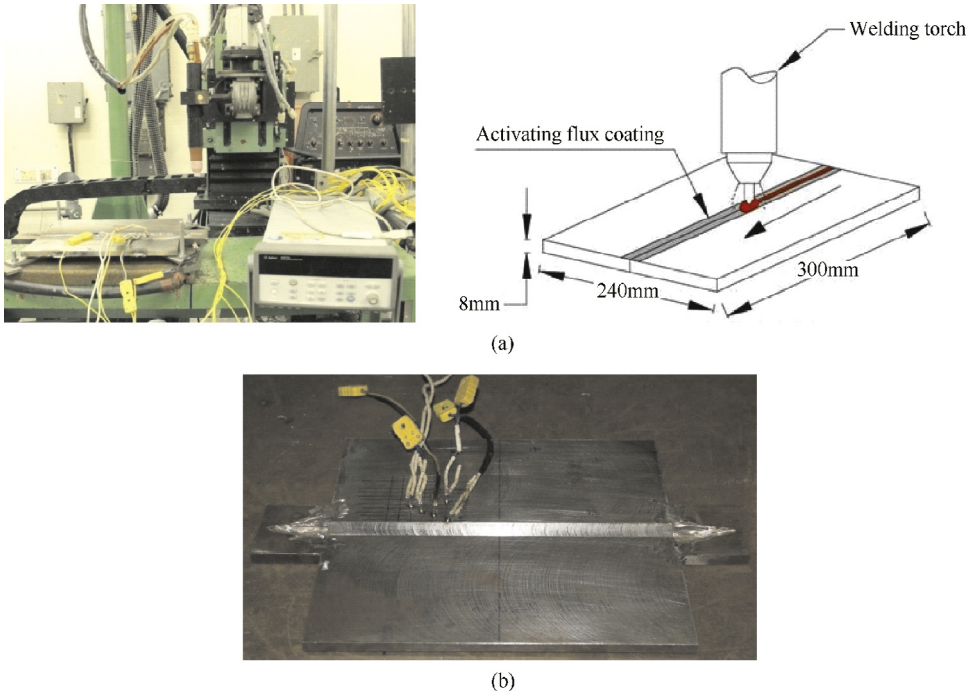

Fig. 2. Spot welded thermocouple (a) A-GTAW joint (b) SMAW joint.

The measurement of residual stresses by Ultrasonic Testing involves selection of weld joint, determination of Acousto-Elastic Constant (AEC) i.e. change in speed or transit time of sound by applying varying loads on tensile specimen, ultrasonic velocity measurements in the weld joint and calculation of residual stresses using AEC. A 2 MHz probe with transmitter angle of 28° (first critical angle for steels) was used to generate longitudinal critically refracted (L_{CR}) waves. The waves have penetration depth of approximately 3 mm. The AEC for DMR-249A steel was calculated to be 0.069 ns/MPa. To measure transit time on the surface of the weld joint using the Ultrasonic probe, grid lines were marked parallel to the weld seam at regular interval of 5 mm starting from 15 mm away from the weld center line at each side of the weld seam.

The XRD was carried out using Cr-Kα radiation X-ray tube operating with a target current of 7 mA at 30 kV (Model: Rigaku MSF 2M). The ψ angles were tilted in steps of 9° in the range of 0° to 45°. The residual stresses were estimated using the peak shift at ψ angles and d-spacing relationship of (211) plane. Scanning was done in the angular range of 150° to 162° in steps of 0.2° with a dwell time of 3 sec at each step to. The Young's modulus of the DMR-249A is taken as 210 GPa to estimate the residual stress values. The calculation of residual stresses based on the shift in the peak position of diffracted X-rays of a selected set of planes is discussed in detail in available literature [19,20].

Numerical model was developed using finite element module SYSWELD. The software is designed to carry out thermo-mechanical analysis of welding as sequentially coupled analysis. The sensitivity of mesh was analyzed by trial and error. The mesh was analyzed using variable mesh size with minimum size near the fusion zone and coarse mesh away from the fusion zone corresponding to the temperature gradient in the welded plates. Two different FE models were generated. The model was taken at the *XY* plane and the welding path parallel to the *Y* axis. For A-GTAW square butt joint, FE models for $300 \times 120 \times 10$ mm^3 size plate was generated with 76,440 elements/82,830 nodes. The symmetric model was mirrored. For SMAW 70° V-Groove butt joint FE model for $300 \times 240 \times 10$ mm^3 plates with included V-Groove at centerline was modeled with 103,350 elements/113,099 nodes. The FE models are shown in Fig. 3.

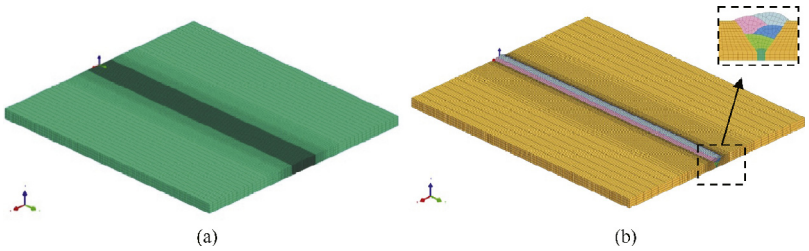

Fig. 3. FE model of weld joint (a) A-GTAW (b) SMAW.

The simulation consisting of thermo-metallurgical analysis and mechanical analysis requires temperature and phase dependent material properties. For thermal analysis; thermal conductivity, specific heat, coefficient of thermal expansion and density with respect to temperature is considered. For mechanical analysis; Young's Modulus, ultimate tensile Strength, Poisson's ratio with respect to temperature are considered. The available properties of equivalent HSLA steel with comparable chemical composition and mechanical properties were used to carry out simulations [18].

During welding, most of the heat energy dispersed into the component by conduction mode heat transfer. In this model, the conduction heat transfer based welding simulation was undertaken by decoupling the welding arc from the welding component. The molten pool stirring was suppressed and the problem was considered as conduction heat transfer analysis. The thermal conductivity of the molten pool after melting point was artificially doubled to consider the molten pool stirring effect. The heat source model used represents the total volumetric heat flux generated by the molten weld pool irrespective of welding process. In FEA model, combined convection and radiation loss was considered as one of the boundary conditions. The model is considered as a "conduction model", because the localized melting and solidification phenomenon was not directly incorporated. In this FEA model, the liquid phase of weld pool was not formed, whereas the shape of molten pool and appropriate volumetric heat flux was represented using double ellipsoidal heat source. The major heat transfer took place in conduction heat transfer mode to the base metal. The convective heat transfer coefficient was taken as 25 W/m^2. The elastic constraints with 1000 N/mm stiffness were applied for nodes/elements.

The filler metal deposition was considered by activating each pass one by one during the simulation. The model was created with base plate and individual bead as an assembly model. In the solver when the simulation was set up, start and end time for each welding pass was appropriately given to maintain the inter-pass temperature. The remaining weld bead was deactivated when a welding pass was being carried out. Later the next bead was activated when the inter pass temperature reached a certain value. During the experiment the clamp was placed on the top of the plate such that it would not move in the vertical direction whereas the horizontal and transverse direction was allowed to expand. Similarly the model was assigned with the clamp that only restrains the plate in vertical direction.

3. Theory/calculation

3.1. XRD equations

The residual strain present in the atomic planes is measured using XRD technique. The change in inter planer space "d" due to residual stress is measured by shift in peak intensity. The residual stress is calculated by using the relation

$$\varepsilon = (d - d_0)/d_0 \tag{1}$$

$$\sigma = (E/1+\upsilon)\times(1/\sin^2\Psi)\times\varepsilon \tag{2}$$

where d_0 is the strain free inter planner spacing, ε is the calculated strain and angle Ψ is the angle between the surface normal and the strain measurement direction.

3.2. Numerical simulation theory

The assumption of welding heat source model for heat generation source in process is essential to simulate a welding process. One of the major characteristics of the heat source is its motion through time and space. Depending on the welding processes and weld bead profiles, volumetric heat sources of double ellipsoidal [12–14,21], semi-spherical [22], 3D conical [23] and combination of heat sources [5] have been widely used for the conduction mode welding simulation. The double ellipsoidal heat source can be used for shallow or high penetration welding process by adjusting its parameters [21]. As the present experiments involve high penetration welding (A-GTAW) and shallow penetration/deposition welding (SMAW), a common heat source model (double ellipsoidal) to compare the integrity of both welding processes was used. The "double ellipsoidal" heat source model [21] is shown in Fig. 4.

The volumetric heat flux within two different ellipsoid (for any point x,y,z) is described by Eqs. (3) and (4). The semi-ellipsoids of different heat flux are combined to give the heat source.

$$Q_f(x,y,z) = \frac{6\sqrt{3}r_f Q}{abc_f\pi\sqrt{\pi}}\exp\left(-\frac{3z^2}{c_f^2}-\frac{3x^2}{a^2}-\frac{3y^2}{b^2}\right) \tag{3}$$

$$Q_r(x,y,z) = \frac{6\sqrt{3}r_r Q}{abc_r\pi\sqrt{\pi}}\exp\left(-\frac{3z^2}{c_r^2}-\frac{3x^2}{a^2}-\frac{3y^2}{b^2}\right) \tag{4}$$

$$\text{Arc heat input, } Q = V\times I\times n \tag{5}$$

where $\boldsymbol{a}$, $\boldsymbol{b}$, $\boldsymbol{c_f}$ and $\boldsymbol{c_r}$ are the geometric parameters of ellipsoidal heat source, shown in Fig. 4.

Q = Heat input in Watts, V = Voltage in Volts and I = Current in Amperes.

The parameters $\boldsymbol{r_f}$ and $\boldsymbol{r_r}$ are proportion coefficients representing heat apportionment in front and back of the heat source respectively, where $\boldsymbol{r_f} + \boldsymbol{r_r} = 2$. It is of great importance to note that the values of $Q(x, y, z)$ given by Eqs. (3) and (4) must be

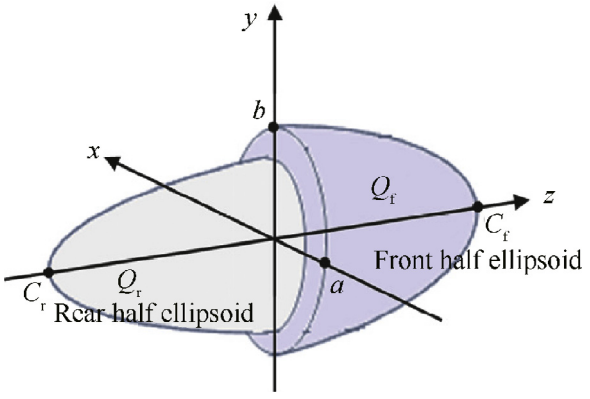

Fig. 4. Heat source model.

equal at the $x = 0$ plane to satisfy the condition of continuity of the overall volumetric heat source. This leads to definition of two constraints $r_f = 2c_f/(c_f + c_r)$ and $r_r = 2c_r/(c_f + c_r)$ such that $r_f/c_f = r_r/c_r$. However, the "double ellipsoidal" model is described by arc efficiency η, and four geometric parameters a, b, c_f and c_r.

4. Results

Experimentally measured macro bead profile and simulated bead profile for A-GTAW and SMAW weld joints are shown in Figs. 5 and 6 respectively. The heat source was calibrated to achieve the bead profile as observed in macro cut section of the welded joints. The heat source parameters were measured from experimentally observed weld attributes and used in the calibration process. Dimensions of heat source were adjusted till it matched with the experimentally observed weld bead. The heat source fitting parameters used for FEM simulation of A-GTAW and SMAW joints are given in Table 3. Figs. 5 and 6 show close agreement between simulated and experimental weld bead profiles.

The experimental validation of temperature distribution was carried out by physically measuring temperature on plate surface using thermocouples placed at 10 mm, 15 mm and 20 mm away from the weld bead. Figs. 7 and 8 shows the validation of predicted thermal cycles in A-GTAW and SMAW process respectively.

Table 3
Values of heat source calibrated function.

Parameter	A-GTAW	SMAW
Front length of the molten zone, A_f/mm	4.5	5.5
Rear length of the molten zone, A_r/mm	9.0	5.0
Half of the width of the bead, B/mm	5.0	3.0
Penetration of the bead, C/mm	6.0	3.0
X,Y,Z	0,0,0	0,0,0
Power/kW	5.4	2.0
Efficiency	0.75	0.65
Velocity/(mm·s^{-1})	1	1.5

Figs. 7 and 8 indicate higher temperature gradients at areas closer to the welding heat input and lower temperatures away from the weld center. The highest heating and cooling rate is observed at the weld center point. The thermal cycle has a steep rise in the curve gradient and the slope of curve is lesser for cooling after the heat source passes, validating higher heating rate than the cooling rate.

The heating rate for both experimental and simulated results was observed to be similar. Figs. 7 and 8 exhibit that the experimental cooling rate was lesser than the simulated cooling rate. It was also observed that thermocouple readings are lower near to weld centerline as compared to FEM but higher as distance from centerline increases, showing higher cooling rate in FEM. The simulated thermal profile showed steeper slope

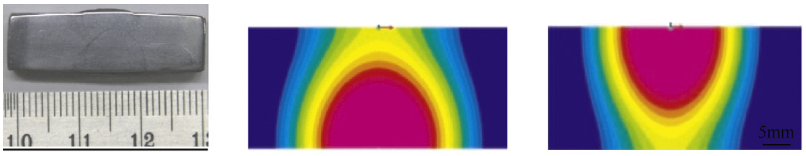

Fig. 5. A-GTAW bead profile (a) Macro (b) First pass (c) Second pass.

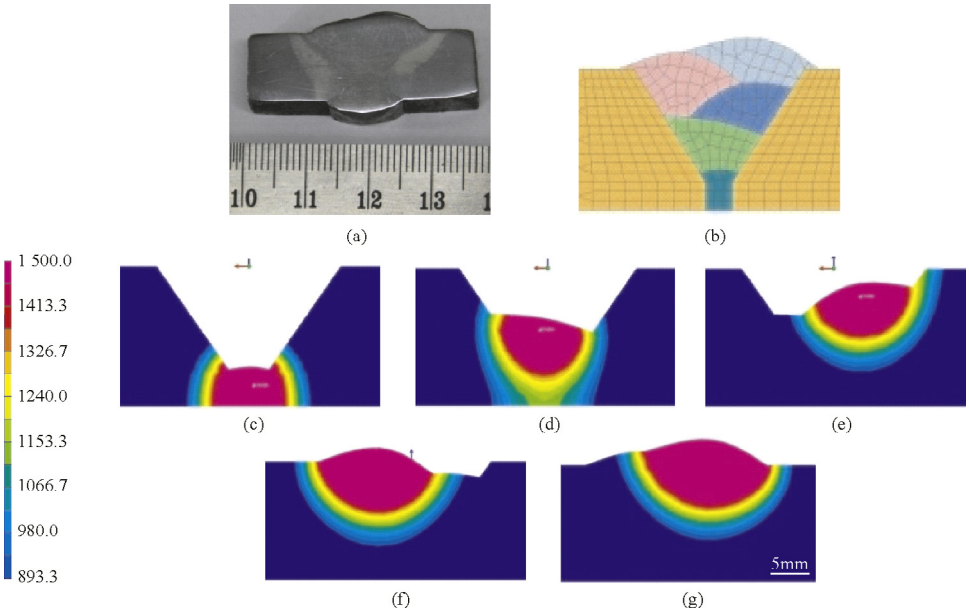

Fig. 6. SMAW bead profiles (a) Macro (b) 5 passes meshing (c)–(g) Passes 1 to 5.

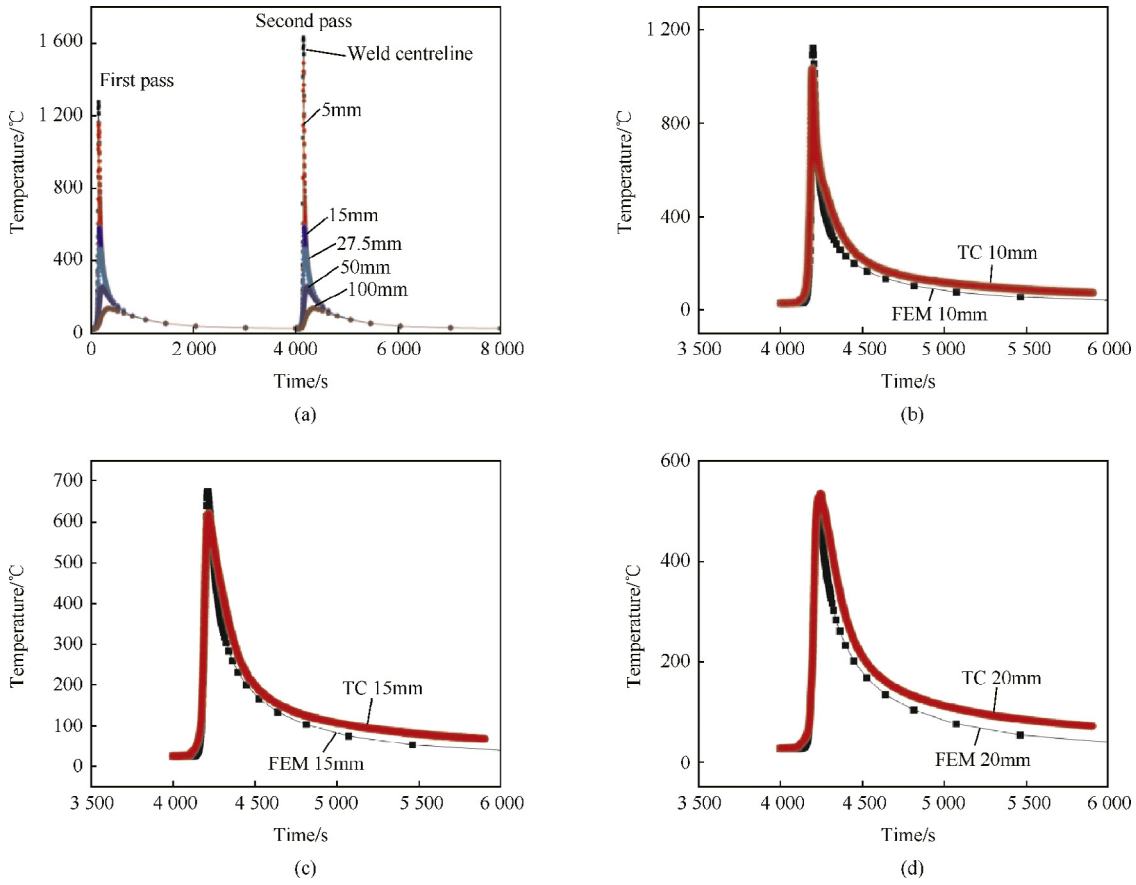

Fig. 7. A-GTAW Thermal cycle (a) transverse direction, (b) at 10 mm, (c) at 15 mm, (d) at 20 mm.

and higher cooling rate as the heat transfer mode was assumed to be primarily conduction with modified higher thermal conductivity for molten weld pool.

The comparison of peak temperature values for each pass measured at the predetermined locations of thermocouple and as deduced from the FEM of A-GTAW and SMAW processes is given in Table 4.

The maximum peak temperature measured at molten weld cenetr in FEM for A-GTAW and SMAW depict the melting temperature and was found to be similar as mentioned in Table 4. The difference between maximum temperatures observed at different distances from weld center for A-GTAW and SMAW is attributed to the difference in heat input for the two welding techniques. The higher heat input of 5 kJ/mm for A-GTAW compared with 2 kJ/mm for SMAW process resulted in higher temperatures in the A-GTAW welded plate. Also, the cooling rate decreases at large heat inputs so that larger quantities of Widmanstatten ferrite are obtained with corresponding reduction in the amount of acicular ferrites. Widmanstatten structure is characterized by its low impact values so the A-GTAW weld joint is expected to have lower impact toughness value at sub zero temperatures as compared to SMAW weld joint.

Table 4
Comparison of peak temperatures measured by thermocouple and FEM.

Distance from weld center	Center line	10mm	15mm	20mm
A-GTAW				
Thermocouple/°C	–	1080	631	541
FEM/°C	1630	1120	683	507
SMAW				
Thermocouple/°C	–	551	381	349
FEM/°C	1579	557	379	318

The residual stress profile in the A-GTAW and SMAW process are given in Fig. 9(a)–(b). The residual stresses as measured experimentally using XRD, UT (Lcr) techniques and FEM simulation for plates using A-GTAW and SMAW processes are shown in Fig. 10.

The various studies on RS measurements reported existence of maximum tensile RS generally up to yield stress of the base material or even up to values matching the tensile strength. RS of 250 MPa for 2219 Al, 300 MPa in 316LN steel, 320 MPa in 316L and 750 MPA in Z8CD12 steels have been reported [24–27]. In Fig. 10(a)–(b), the tensile RS are shown to be present up to 20 mm to 40 mm on either side of the weld line.

Fig. 10 and Table 5 show that experimental stress measurements are comparable with the numerical prediction. The profiles of the residual stresses measured experimentally and using FEM were observed to be similar. The minor variations in absolute values of stresses is attributable to the difference in residual stress gradients for different welding techniques and inherent volume of inspection of surface and bulk residual

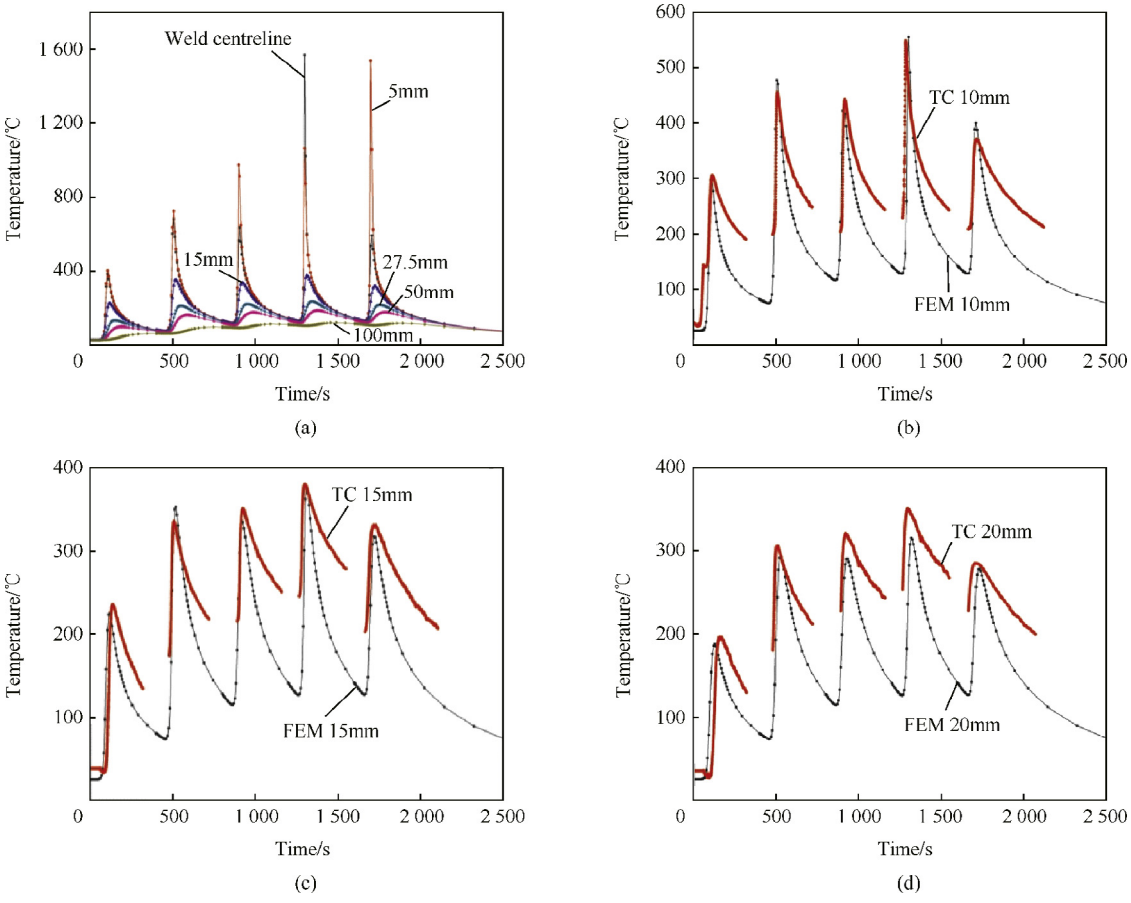

Fig. 8. SMAW Thermal cycle (a) transverse direction, (b) at 10 mm, (c) at 15 mm, (d) at 20 mm.

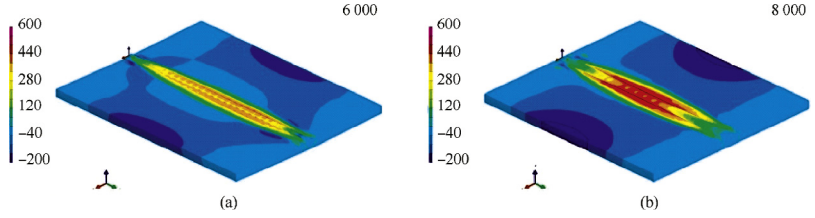

Fig. 9. Simulated longitudinal stress using FEM (a) A-GTAW (b) SMAW.

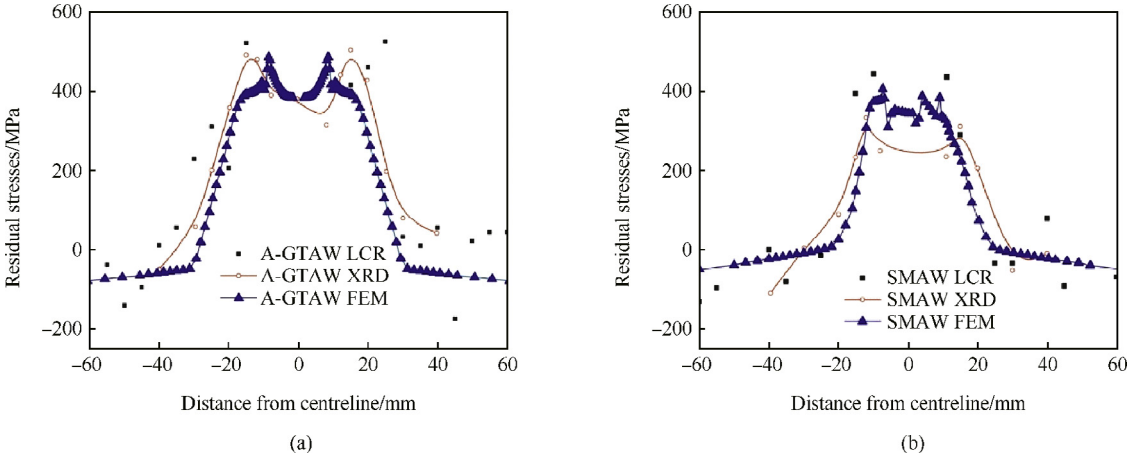

Fig. 10. Residual stress comparison of FEM with XRD and LCR methods (a) A-GTAW (b) SMAW.

Table 5
Comparison of maximum residual stress (MPa).

	Experimental	FEM
A-GTAW	526	496
SMAW	450	407

stresses of respective technique [5–14,19,20]. The XRD measurements are sensitive to surface conditions with assumed depth of penetration in the order of 5 to 30 microns. For the L_{CR} measurements, residual stress is the average value over effective penetration of 3 mm. The FEM simulated values are average stress values interpreted from the SYSWELD model.

The microstructure studies of base metal DMR-249A and arc welded joints were undertaken using optical microscope. The microstructure of base metal and weld metal of different arc welded joints at 500× magnification are given in Fig. 11. The microstructure of base metal show predominantly fine grained equiaxed ferrite and some percentage of banded structured pearlite. For weld metals, the optical images showed arc welded joints with grain boundary ferrite, Widmanstatten ferrite with aligned second phase along with veins of ferrite, acicular ferrite, polygonal ferrite and microphases. The grain boundary ferrite has equiaxed form or thin veins delineating prior austenite grain boundaries. The sideplate Widmansttten ferrite is seen as the parallel ferrite laths emanating from prior austenite grain boundaries.

The M-Shape profile for measured RS may be attributed to the phase transformation occurring during solid state transformation of equiaxial ferrite in base material to grain boundary ferrite, accicular ferrite, Widmanstatten ferrite, bainite and micro alloying phases, which causes volume changes in weld metal. The volume expansion due to phase transformation counters the volume contraction due to shrinkage, releasing the tensile RS. The RS induced by shrinkage of the molten region are usually tensile. The compressive residual stresses are formed in the transformed areas where the effect of phase transformations is dominant. The area fractions of various ferritic morphologies seen in optical images were ascertained with systematic manual point counting as per ASTM E 562. The SMAW exhibited higher percentage of microphases and polygonal ferrite and A-GTAW associated with high heat input was observed to contain about more of Widmanstatten ferrite. The volume fractions of grain boundary ferrite, Widmanstatten ferrite, polygonal ferrite and microphases for the SMAW and A-GTAW weld metals are given in Table 6.

Table 6
The volume fraction of grain boundary ferrite, Widmanstatten ferrite, polygonal ferrite and microphases using manual point counting.

Volume fraction	Grain boundary ferrite/G	Widmanstatten ferrite/W	Polygonal ferrite/P	Microphases
SMAW	20	09	15	56
A-GTAW	19	24	09	48

The transformation of austenite to these ferritic morphologies are distinguished by the atomic mechanism of transformation as reconstructive (grain boundary/polygonal ferrite) and displacive (Widmanstatten, acicular and bainitic ferrites). While reconstructive transformation is associated with volume change, the displacive transformation is accompanied by invariant plane strain (IPS) [28–31]. The M-Shape profile for measured RS is attributed to the volume fraction changes due to transformation of equiaxial ferrite in base material to Grain Boundary Ferrite, Accicular Ferrite, Widmanstatten Ferrite, bainite and micro alloying phases in weld metal [32,33]. The marginally higher residual stresses in A-GTAW as compared to SMAW is attributed to higher percentage of displacively transformed Widmanstatten ferrite and microphases (combination of acicular ferrite and bainite) in A-GTAW weld metal and also expected formation of higher percentage of bainite in HAZ due to higher heat input and slower cooling rates [34]. The presence of higher percentage of reconstructively transformed grain boundary and polygonal ferrite in SMAW as compared to A-GTAW resulted in volume change in weld metal, leading to reduction in tensile residual stresses at weld center. A-GTAW being an automated process, the variations in experimentally measured residual stresses and derived from FEM were observed to be minimal (Fig. 11(a)). Minor variation in residual stress values of experimental measurements and FEM for SMAW (Fig. 11(b)) is due to manual process being used. For SMAW, there is minor variation in the location of passes in experiment and FEM. Also, the energy absorbed during SMAW not being uniform might have impacted the field under stress.

The impact toughness, with notch in weld metal, was carried out at room temperature for SMAW and A-GTAW joints. The impact toughness was found to be 150 J and 200 J for SMAW and A-GTAW joints respectively. The tensile test performed on

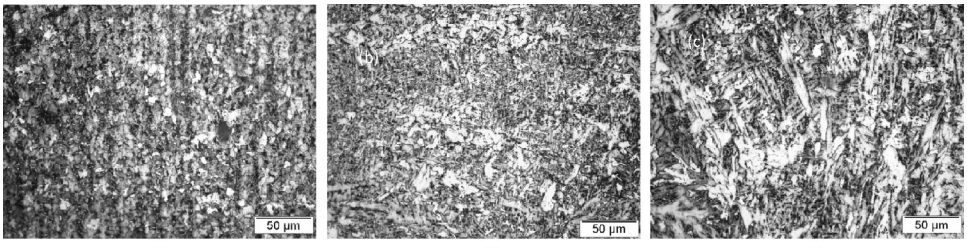

(a) (b) (c)

Fig. 11. Optical (500×) images of base metal and weld joints (a) DMR 249A (b) SMAW (c) A-GTAW.

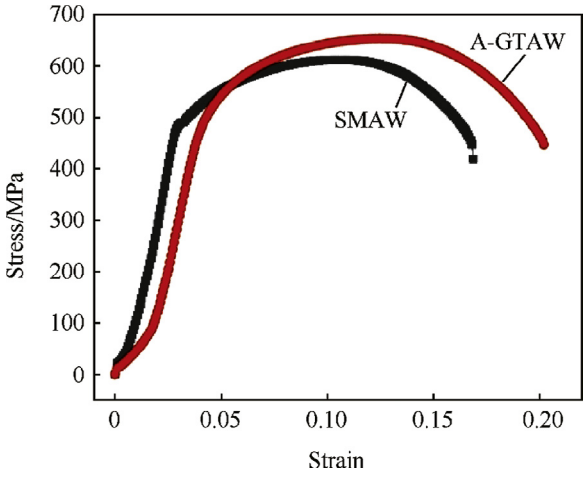

Fig. 12. Stress vs Strain curve for SMAW and A-GTAW cross weld specimen.

cross weld specimen of both joints has shown comparable yield strength of about 480 MPa and percentage elongation of 20% but the ultimate tensile strength of 640 MPa in G-TAW specimen was higher as compared to about 600 MPa of SMAW specimen (Fig. 12). The tensile fracture of the cross weld specimen of SMAW and A-GTAW occurred in the base metal region away from weld metal which confirmed the existence of adequate strength in weld metal of both processes. The comparison of mechanical tests of SMAW and A-GTAW joints are given in Table 7.

The fractography studies of tensile specimen and V-notch Chapry impact specimen for both the arc weld joints revealed ductile fracture with characteristic cup and cone dimples structure. The fractography studies confirmed and corroborated the high values measured for UTS and impact tests as given in Table 7 above. The fractured tensile and impact specimens with scanning electron microscope images are shown in Figs. 13 and 14 respectively.

Table 7
Comparison of mechanical tests of SMAW and A-GTAW joints.

Weld joint	Elongation/%	YS/MPa	UTS/MPa	Impact toughness/J (Room temp)
SMAW	20	480	640	150
A-GTAW	20	480	610	200

The micro hardness values measured across the weld joint at 2 mm and 5 mm below the surface for SMAW and A-GTAW joints is shown in Fig. 15. In SMAW joint, hardness was found between 200 and 330 $HV_{0.2}$ whereas for A-GTAW joint hardness was within the scatter band of 200–280 $HV_{0.2}$. The profile of hardness across the weld joint for both joints was observed to be similar. The hardness of weld metal was measured to be higher than the base metal. The micro-hardness values gradually increases from base metal to HAZ and a minor decrease in the hardness value was observed near the fusion zone followed by higher hardness values in weld metal.

5. Conclusions

The thermo-mechanical behavior of DMR-249A steel weld joints manufactured by SMAW and A-GTAW processes were studied using Finite Element Model (FEM) simulation. The conclusions based on the present investigations are summarized as follows:

1) The thermo-mechanical characteristics of A-GTAW and SMAW for DMR-249A steel were investigated using

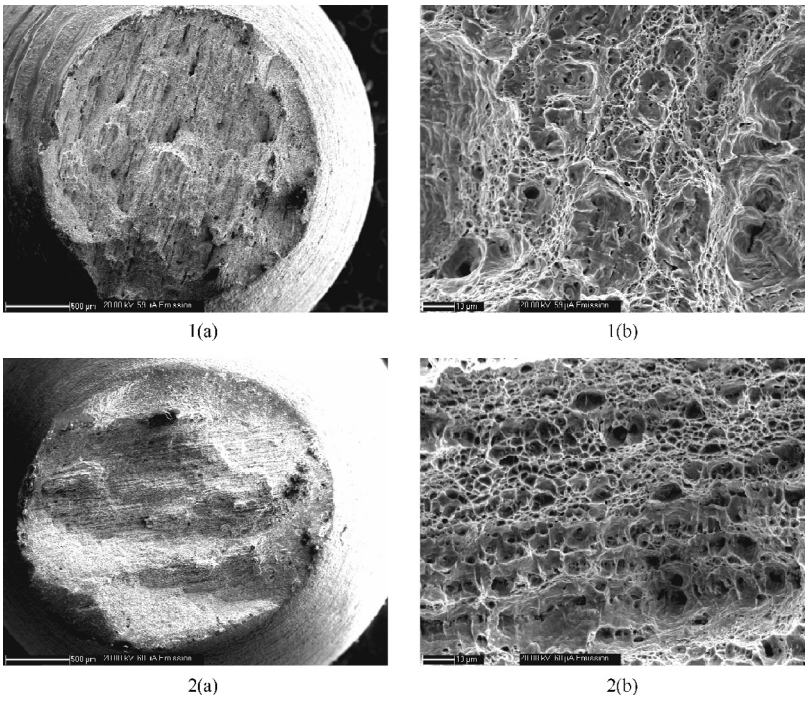

Fig. 13. Fractured tensile test specimen images (1) SMAW (2) A-GTAW.

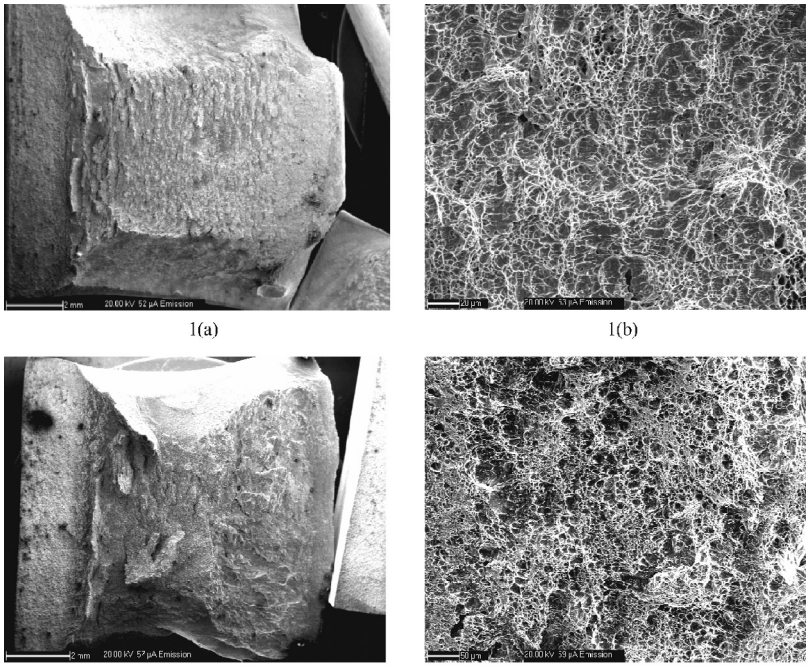

Fig. 14. Fractured V-notch Charpy impact specimen images (1) SMAW (2) A-GTAW.

numerical modeling and experimentally validated using non destructive testing.

2) The higher heat input of 5 kJ/mm for A-GTAW compared with 2 kJ/mm for SMAW process resulted in higher temperatures in the A-GTAW welded plate. Also, the arc constriction in A-GTAW induces concentrated temperature at the welding center line which attributes higher temperature. The measured and predicted thermal cycles for both the weld joints fabricated by SMAW and A-GTAW processes were observed to be comparable.
3) The results presented by numerical models were consistent with the practical measurements by XRD and Ultrasonic Testing. The M-Shape profile for measured residual stress is attributed to the phase transformation occurring during transformation of equiaxed ferrite in base material to grain boundary ferrite, accicular ferrite, Widmanstatten ferrite, bainite and micro alloying phases which cause invariant plane strain and volume changes in weld metal.
4) The study establishes reliability of FEM based thermo-mechanical analysis for interpretation of thermal cycles and residual stress in DMR-249A steel weld joints.
5) Considering high productivity and savings of cost and labor associated with A-GTAW process, the minor variation of residual stresses buildup in A-GTAW joint can be

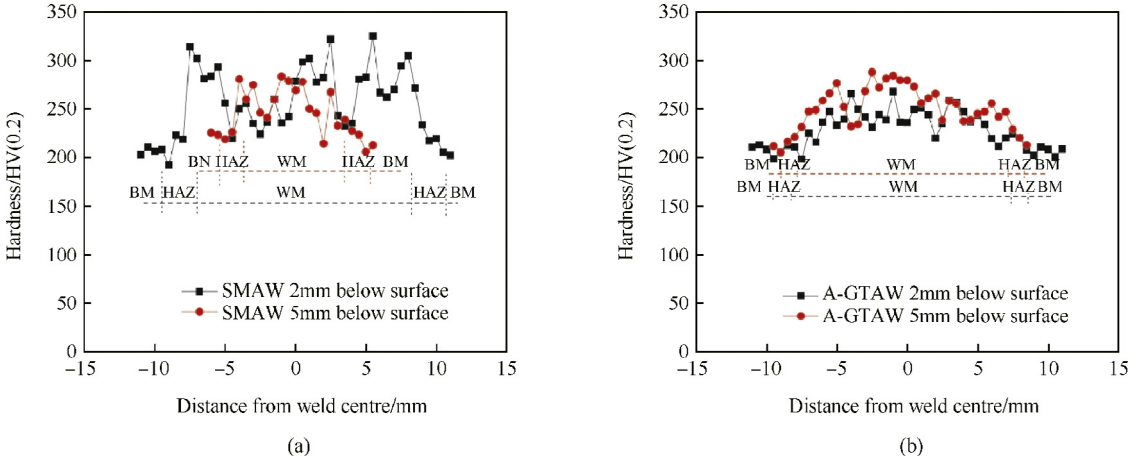

Fig. 15. Micro-hardness profile across weld joints (a) SMAW (b) A-GTAW.

ignored to develop A-GTAW as qualified alternative welding technique for DMR-249A.

Acknowledgement

The authors express gratitude to the Indian Navy, Mazagaon Dockyard Limited, Mumbai and Cochin Shipyard Limited, Kochi for their constant encouragement and support. Authors would like to thank Dr GK Sharma, Mr S Mahadevan and Mr Arun Kumar for the help extended during residual stress measurements. Authors would also like to express sincere thanks to Dr. BPC Rao for extending the facilities at NDED, IGCAR to conduct the experiments and studies.

References

[1] Mallik S, Minz BS, Mishra B. Production of DMR-249A steel at SAIL, bokaro steel plant. Mater Sci Forum 2012;710:149–54.
[2] Malakondaiah G. Development of speciality low alloy steels, international conference on metals and alloys: past, present and future, December 7–10, 2007, pp. 17.
[3] An international patent Tungsten Inert Gas Welding Flux for enhancing Penetration in Single Pass for austenitic stainless steels, Patent no. PCT/IN06/00442/dt. 8/11/06.
[4] Pamnani R, Vasudevan M, Vasantharaja P, Jayakumar T. Optimisation of A-GTAW welding parameters for naval steel (DMR-249A) by design of experiments approach. Proc Inst Mech Eng L J Mater Des Appl 2015; doi:10.1177/1464420715596455.
[5] Chukkan JR, Vasudevan M, Muthukumaran S, Ravi Kumar R, Chandrasekhar N. Simulation of laser butt welding of AISI 316L stainless steel sheetusing various heat sources and experimental validation. J Mater Process Technol 2015;219:48–59.
[6] Mochizuki M. Control of welding residual stress for ensuring integrity against fatigue and stress–corrosion cracking. Nucl Eng Des 2007; 237:107–23.
[7] Dong P, Brus FW. Welding residual stresses and effects on fracture in pressure vessel and piping components: a millennium review and beyond. J Press Vessel Technol 2000;122:329–38.
[8] Lin Q, Chen J, Chen H. Possibility of inducing compressive residual stresses in welded joints of SS 400 steels. J Mater Sci Technol 2001;17(6):661–3.
[9] Bate SK, Green D, Buttle D. A review of residual stress distribution in welded joints for defect assessment of offshore structures. HSE Books, AEA Tech PLc; 1997.
[10] Pamnani R, et al. Residual stress studies on arc welding joints of naval steel (DMR-249A). J Manuf Process 2015;doi:10.1016/j.jmapro .2015.09.004.
[11] Vasantharaja P, Maduarimuthu V, Vasudevan M, Palanichamy P. Assessment of residual stresses and distortion in stainless steel weld joints. Mater Manuf Process 2012;27:1376–81.
[12] Ravisankar A, Velaga SK, Rajput G, Venugopal S. Influence of welding speed and power on residual stress during gas tungsten arc welding (GTAW) of thin sections with constant heat input: a study using numerical simulation and experimental validation. J Manuf Process 2014; 16(2):200–11.
[13] Velaga Satish K, et al. Comparison of weld characteristics between longitudinal seam and circumferential butt weld joints of cylindrical components. J Manuf Process 2015;18:1–11.
[14] Ganesh K, Vasudevan CM, Balasubramanian KR, Chandrasekhar N, Vasantharaja P. Thermo – mechanical analysis of TIG welding of AISI 316LN stainless steel. Mater Manuf Process 2014;29(8):903–9.
[15] Alghamdi T, Liu S. Low transformation temperature welding consumables for residual stress management: a numerical model for the prediction of phase transformation-induced compressive residual stresses. Weld J 2014;93(12):458s–71s.
[16] Duranton P, Devaux J, Robin V, Gilles P, Bergheau JM. 3D modelling of multi pass welding of A 316L stainless steel pipe. J Mater Process Technol 2004;153–154:457–63.
[17] Mollicone P, Camilleri D, Gray TGF, Comlekci T. Simple thermo-elastic–plastic models for welding distortion simulation. J Mater Process Technol 2006;176:77–86.
[18] Srikas T, Papanikos P, Kermanidis T. Numerical simulation of laser welding process in butt joints joint specimens. J Mater Process Technol 2013;134(1):59–69.
[19] Cullity BD, Stock SR. Elements of X-ray diffraction. 1st ed. New Jersey: Prentice Hall; 2001.
[20] Raj B, Jaykumar T, Mahadevan S, Rai SK. X-ray diffraction based residual stress measurement for assessment of fatigue damage and rejuvenation process for undercarriages of aircraft. J Nondestruct Eval 2009;28(3–4):157–62.
[21] Goldak JA, Chakravarti A, Bibby M. A finite element model for welding heat sources. Met Trans B 1984;15B:299–305.
[22] Liu C, Zhang JX, Xue CB. Numerical investigation on residual stress distribution and evolution during multipass narrow gap welding of thick-walled stainless steel pipes. Fusion Eng Des 2011;86:288–95.
[23] Heinze C, Schwenk C, Rethmeier M. Effect of heat source configuration on the result quality of numerical calculation of welding-induced distortion. Simul Model Pract Theory 2012;20:112–23.
[24] Lu H X., Liu S, Yang JG, Zhang SP, Fang HY. Ultrasonic stress evaluation on welded plates with L_{CR} wave. STWJ 2008;13:70–4.
[25] Gilles P, El-Ahmar W, Jullien J-F. Robustness analyses of numerical simulation of fusion welding NeT-TG1. Int J Pres Ves Pip 2009;86:3–12.
[26] Pratihar S, Turski M, Edwards L, Bouchard PJ. Neutron diffraction residual stress measurements in A 316L stainless steel bead-on-plate weld specimen. Int J Pres Ves Pip 2009;86:13–19.
[27] Belahcene F, Lu J. Determination of residual stress in Z8CDWV12 steel using critically refracted longitudinal waves. JSME Int J A Solid M 2000;43(4):367–73.
[28] Withers PJ, Bhadeshia HKDH. Residual stress: part 1. J Mater Sci Technol 2001;17:355–65.
[29] Withers PJ, Bhadeshia HKDH. Residual stress: part II. J Mater Sci Technol 2001;17:366–75.
[30] Dai H, Francis JA, Stone HJ, Bhadeshia HKDH, Withers PJ. Characterizing phase transformations and their effects on ferritic weld residual stresses with X-rays and neutrons. Metall Mater Trans A 2008; 39A:3070–8.
[31] Bhadeshia HKDH. Effect of Materials and Processing-ASM Handbook of Residual Stress and Deformation of Steel 2002.
[32] Rossini NS, Dassisti M, Benyounis KY, Olabi AG. Methods of measuring residual stresses in components. Mater Des 2012;35:572–88.
[33] Totten GE. Handbook on residual stress, vol. 1. ASM International; 2002. p. 417.
[34] Bose-Filho WW, Carvalho ALM, Strangwood M. Effect of alloying elements on the microstructure and inclustion formation in HSLA multipass welds. Mat Charac 2007;58:29–39.